Article

Bone-targeted celastrol nanocarrier suppresses osteoclastogenesis in postmenopausal osteoporosis

Check for updates

Xiaolong Yu[1], Shengtao Zhang[1], Zhiqi Wei[1] & Qiang Xu[1,2] ✉

Osteoporosis is a metabolic disorder characterized by progressive bone loss, particularly affecting postmenopausal women. Excessive osteoclast activity contributes to bone resorption and skeletal fragility. Celastrol, a natural triterpene, has demonstrated anti-inflammatory and anti-resorptive effects, but its clinical application is limited by poor solubility and systemic toxicity. In this study, we engineered a bone-targeted nano-sustained-release system using mesoporous silica nanoparticles loaded with celastrol. The nanocarrier displayed high bone affinity, sustained drug release, and favorable biocompatibility. In vitro, it suppressed RANKL-induced osteoclast formation and function by downregulating NF-κB and MAPK signaling. In vivo, treatment of ovariectomized rats improved bone mineral density, preserved trabecular microarchitecture, and reduced osteoclast numbers without apparent systemic toxicity. These findings demonstrate that bone-targeted celastrol nanoparticles provide an efficient and safe therapeutic strategy for postmenopausal osteoporosis by inhibiting osteoclastogenesis and protecting bone structure.

Osteoporosis (OP) is a progressive skeletal disorder among the elderly population, and with the increasing trend of aging populations worldwide, its impact is becoming more prominent[1–3]. In particular, the incidence of OP is higher in postmenopausal women, with one in every two women over the age of 50 in the United States expected to experience an osteoporotic fracture. Postmenopausal women face an increased risk for both vertebral and non-vertebral fractures, as well as a higher likelihood of experiencing subsequent fractures within 1–2 years of the initial event[4]. This is likely related to physiological changes such as bone loss due to declining estrogen levels[5,6]. In addition to reduced bone mineral density and typical symptoms of OP, patients may also suffer from complications such as fractures, loss of height, and postural deformities, all of which can substantially impair their overall quality of life[7–9]. However, in the United States, only 24% of women aged 60 and above receive OP-targeted treatment within the first year after fracture. Conventional treatments rely heavily on pharmacologic interventions, including calcium supplements, vitamin D analogs, and growth hormones[10–12]. Yet, prolonged use of these medications has been linked to adverse effects and diminishing efficacy. While some studies have documented that supplementation with calcium and vitamin D reduces fracture risk[13–15], other studies have shown no such benefit[16–19]. Moreover, calcium supplements may increase the risk of cardiovascular events, gastrointestinal discomfort, and when combined with vitamin D, even nephrolithiasis[20].

Given these limitations, there is an urgent need to identify and advance novel therapeutic approaches[21]. The development of innovative strategies—such as gene therapy and nanodrug delivery systems—may offer alternatives or adjuncts to traditional treatments, broadening therapeutic options and improving efficacy[22].

This study focused on a bone-specific nano-formulated delivery platform incorporating Thunder God Vine Extract and aspartic acid sequences, proposed as a novel therapeutic modality for managing postmenopausal OP. Celastrol has been reported to alleviate OP by inducing osteogenic differentiation of bone marrow-derived mesenchymal stem cells, and by inhibiting osteoclastogenesis and resorption activity through suppression of β-activated kinase 1-mediated activation of the NF-κB and MAPK pathways and downregulation of osteoclast-related genes[23–26]. The research methodology includes advanced nanotechnology synthesis methods and comprehensive evaluation of the performance and mechanisms of action of this sustained-release material in in vitro and in vivo experiments[27,28]. Preliminary results show that this Nano sustained-release material exhibits promising effects in inhibiting osteoclast activity in preventing and treating postmenopausal OP. The therapeutic mechanism is believed to involve suppression of the NF-κB and MAPK axes[29–31].

Furthermore, through in-depth research, we aim to elucidate the mechanisms of action of this bone-targeted nano sustained-release system,

[1]Department of Orthopedics, The First Affiliated Hospital, Jiangxi Medical College, Nanchang University, Nanchang, China. [2]Postdoctoral Innovation Practice Base, The First Affiliated Hospital, Jiangxi Medical College, Nanchang University, Nanchang, People's Republic of China. ✉e-mail: xuqiangyisheng@126.com; ndyfy09659@ncu.edu.cn

providing innovative insights and approaches for OP treatment[32,33]. Our ultimate goal is to develop more effective therapeutic options for post-menopausal OP patients, enhance the understanding of disease pathogenesis, and contribute to advancements in clinical management—ultimately improving patients' quality of life. Here, we strive to foster innovation and progress in the field of OP therapy.

Specifically, this research focuses on exploring the underlying mechanisms by which the nano sustained-release material—loaded with the active extract from *Tripterygium wilfordii* (Thunder God Vine)—exerts its therapeutic effects in postmenopausal OP. Particular attention is given to the roles of the NF-κB and MAPK axes in modulating osteoclast activity. We believe this study will provide critical scientific evidence to support the development of novel OP treatment strategies, leading to improved clinical outcomes and health benefits for affected individuals. By investigating both the mechanisms and therapeutic efficacy of this innovative approach, we aim to offer comprehensive treatment options for OP and contribute to the broader understanding and clinical management of this debilitating disease.

Results

Preparation and characterization of bone-targeted nano-sustained-release materials C@MSN-P-A8

The bone-targeted nanodrug delivery system, C@MSN-P-A8, was synthesized using a modified sol-gel method. As illustrated in Fig. 1A, MSNs were initially prepared using CTAB as a templating agent and TEOS as the silica source. Amination was performed by treating MSNs with APTMS, yielding MSN-NH₂. Celastrol was then loaded into MSN-NH₂ to form Celastrol@MSN, and fluorescein isothiocyanate (FITC) was incorporated to generate fluorescently labeled Celastrol@FITC-MSN-NH₂. Separately, PEG-ASP8 was synthesized by coupling HOOC-PEG-NH₂ with the bone-targeting peptide ASP8 using EDC-mediated condensation. The final product, C@MSN-P-A8, was obtained by grafting PEG-ASP8 onto the surface of Celastrol@FITC-MSN-NH₂.

TEM revealed that MSN, C@MSN, and C@MSN-P-A8 maintained a uniform spherical morphology (Fig. 1B). While MSN exhibited a well-defined mesoporous structure, this structural clarity decreased progressively after drug loading and surface modification, accompanied by an increase in particle diameter. DLS analysis showed hydrodynamic diameters of approximately 120.06 nm (MSN), 136.38 nm (C@MSN), and 173.94 nm (C@MSN-P-A8) (Fig. 1C).

TGA further confirmed material composition changes. Weight loss for MSN, C@MSN, and C@MSN-P-A8 was approximately 7.82%, 15.43%, and 25.54%, respectively (Fig. 1D).

Drug release profiles were evaluated in PBS. Within 42 h, C@MSN released nearly 60% of Celastrol, demonstrating a burst release pattern. In contrast, C@MSN-P-A8 showed a slower, more controlled release, with ~30% of Celastrol released over the same period, suggesting effective sustained-release characteristics (Fig. 1E).

To assess bone-targeting capability, in vivo fluorescence imaging was conducted. At 4 h post-injection, similar fluorescence signals were observed in major organs for all nanoparticle formulations. However, at 72 h, MSN and C@MSN were largely cleared from the liver and kidneys, while the C@MSN-P and C@MSN-P-A8 groups exhibited stronger retention. Notably, only the C@MSN-P-A8 group exhibited a markedly stronger fluorescence signal in the femur at 72 h, indicating effective bone-targeted delivery in vivo (Fig. 1F).

Meanwhile, nitrogen adsorption-desorption isotherms of MSN displayed a classical Langmuir type IV curve, confirming the presence of mesoporous structures in MSN (Fig. 2A). The pore size distribution, derived from the adsorption branch, confirmed capillary condensation in the range of 0.8–1.0 relative pressure (Fig. 2B). The specific surface area and average pore diameter of MSN were calculated to be 875.21 m²/g and 3.57 nm, respectively.

As illustrated in Fig. 2C, D, C@MSN-P-A8 exhibited no significant cytotoxicity in BMM or RAW264.7 cells at concentrations below 20 μM.
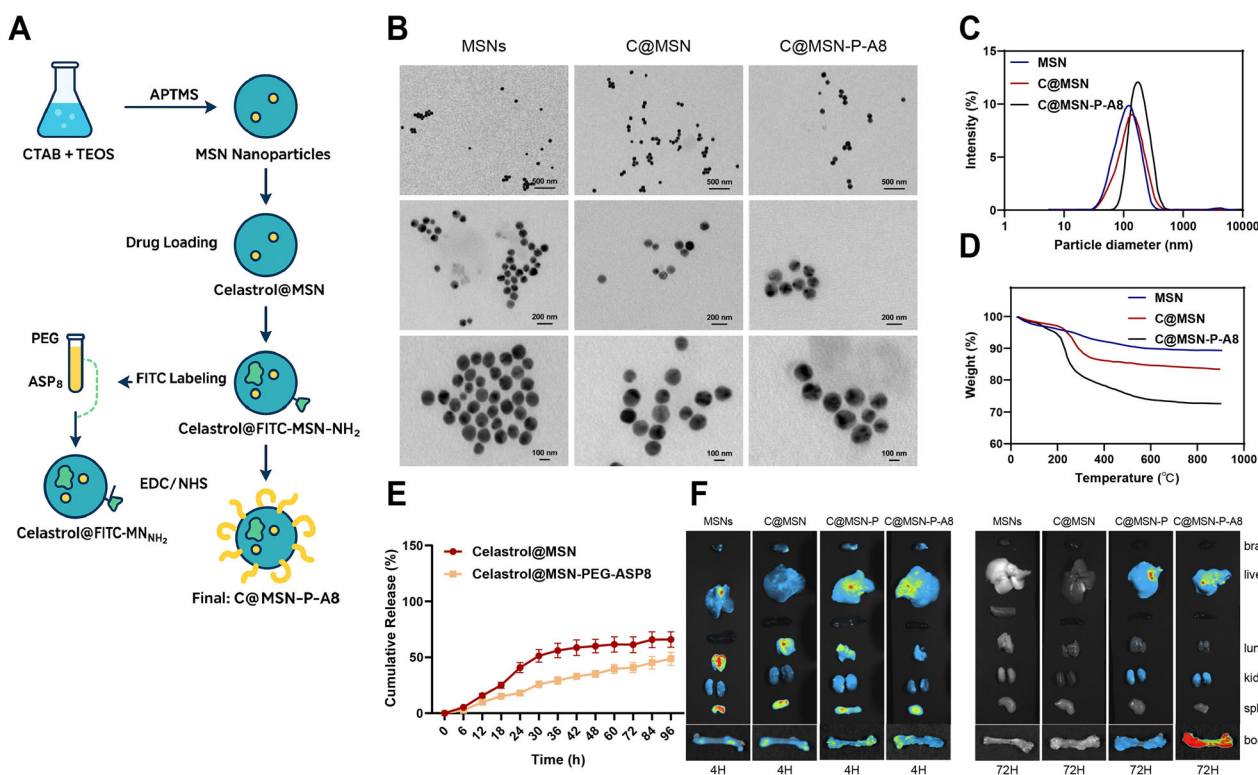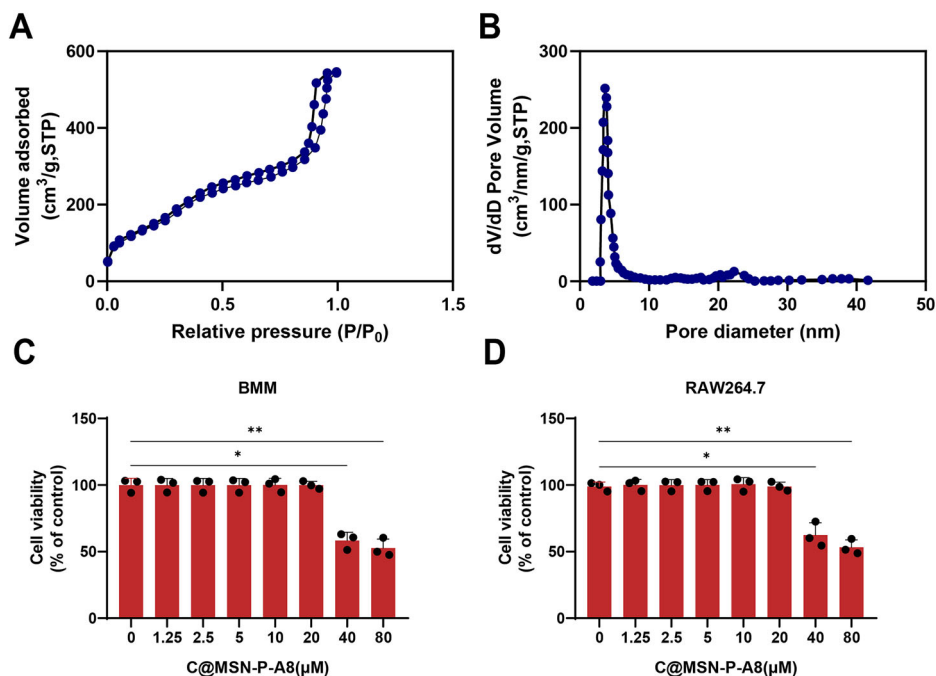

Fig. 1 | Preparation and characterization of C@MSN-P-A8. A Schematic representation of the preparation of C@MSN-P-A8. **B** Typical SEM images of MSNs, C@MSN, and C@MSN-P-A8. **C** DLS curves of MSNs, C@MSN, and C@MSN-P-A8. **D** TGA curves of MSNs, C@MSN, and C@MSN-P-A8. **E** Drug release curve of Celastrol from C@MSN-P-A8. **F** In vivo targeted fluorescence experiment: fluorescence images of various organs at 4 and 72 h post-injection of MSNs, C@MSN, C@MSN-PEG, and C@MSN-P-A8.

Fig. 2 | Characterization of MSN. A N2 adsorption-desorption isotherm of MSN nanoparticles. **B** Pore size distribution curve of MSN nanoparticles. **C** CCK-8 assay showing the impact of C@MSN-P-A8 on the viability of BMMs. **D** CCK-8 assay demonstrating the effect of C@MSN-P-A8 on the viability of RAW264.7 cells. * indicates comparison between the two groups, $P < 0.01$, **$P < 0.01$. Each cell experiment was performed in triplicate.

Collectively, these findings confirm the successful fabrication of a bone-targeted mesoporous silica-based nano delivery system.

Inhibition of osteoclast formation and bone resorption by C@MSN-P-A8

We then focused on the inhibitory potential of C@MSN-P-A8 in osteoclastogenesis. TRAP staining revealed that C@MSN-P-A8 significantly suppressed the formation of TRAP-positive multinucleated osteoclasts in a dose-dependent fashion, without inducing cytotoxicity. In contrast, the untreated control group exhibited numerous large, TRAP-positive multinucleated cells. Quantitative analysis showed a marked decline in both the number and surface area of TRAP-positive osteoclasts upon C@MSN-P-A8 treatment (Fig. 3A). These findings were consistent with results obtained using the RAW264.7 cell line (Fig. 4A).

In addition, F-actin ring formation was disrupted by C@MSN-P-A8 in a concentration-dependent fashion. In control cultures, well-organized, circular F-actin rings were clearly observed. Treatment with increasing concentrations of C@MSN-P-A8 resulted in fewer and morphologically deformed actin rings (Fig. 3B), a trend also confirmed in RAW264.7 cells (Fig. 4B).

Then, the effect of C@MSN-P-A8 on osteoclast-mediated bone resorption was studied. Subsequently, before scanning electron microscopy, toluidine blue staining was performed to better visualize the resorption pits. Bone slices were then treated with different concentrations (0, 2.5, 5, and 10 μM) of C@MSN-P-A8 for 48 h. Scanning electron microscopy revealed substantial reductions in both the number and area of resorption pits on the bone surface in treated groups compared to controls (Fig. 3C, D). Similar anti-resorptive effects were observed in RAW264.7 cells (Fig. 4C, D).

Collectively, C@MSN-P-A8 effectively inhibits both the formation and bone-resorptive activity of osteoclasts in vitro.

C@MSN-P-A8 inhibits osteoclast differentiation by modulating the NF-κB and MAPK Axes

RANKL, a critical cytokine produced in the bone marrow microenvironment, induces the differentiation of osteoclast precursors into mature, bone-resorbing osteoclasts. Upon binding to its receptor RANK, RANKL activates downstream pathways, most notably the NF-κB signaling cascade, which is vital in osteoclastogenesis[34,35]. To evaluate the inhibitory effect of C@MSN-P-A8 on osteoclast-specific gene expression, we conducted RT-qPCR analysis. As expected, RANKL stimulation notably elevated the expression of TRAP, CTSK, and CTR. However, treatment with C@MSN-P-A8 markedly suppressed the mRNA levels of these genes in BMMs (Fig. 5A).

Given that the NF-κB and MAPK pathways are key drivers of osteoclast development and activity[33], we next examined whether C@MSN-P-A8 modulates these pathways. Prior research has shown that Celastrol can inhibit phosphorylation events in both NF-κB and MAPK signaling, thereby attenuating osteoclast differentiation and preventing bone loss in ovariectomized models[36]. Based on this, we assessed the phosphorylation states of key signaling molecules following RANKL stimulation, with or without C@MSN-P-A8 treatment.

In response to RANKL, p-p65 increased at 10 min and declined at later time points (30 and 60 min). In contrast, cells in the RANKL plus C@MSN-P-A8 group exhibited reduced p-p65 expression at both 10 and 30 min, with no significant difference at 60 min relative to the RANKL group. Additionally, IκBα protein levels decreased upon RANKL stimulation at early time points but were partially restored by C@MSN-P-A8. The phosphorylated form, p-IκBα, showed elevated expression at 10 min under RANKL alone, while this effect was significantly attenuated in the RANKL + C@MSN-P-A8 treatment group (Fig. 5B).

For the MAPK signaling cascade, RANKL stimulation led to an elevation in the levels of p-JNK, p-ERK, and p-p38. Notably, the former two were markedly reduced in the C@MSN-P-A8 group. While p-p38 remained elevated at 10 min post-stimulation, its levels declined at 30 min following C@MSN-P-A8 treatment, with no significant change observed at 60 min (Fig. 5C).

To further investigate downstream transcription factors, Western blot analysis was performed to evaluate c-Fos and NFATc1 expression at 0, 1, 3, and 5 days post-treatment. RANKL significantly induced both proteins over time. However, co-treatment with C@MSN-P-A8 brought about a substantial decline in the expression of c-Fos and NFATc1 relative to RANKL alone (Fig. 5D). These effects were reproducible in the RAW264.7 cell line (Supplementary Fig. 1A–D).

Overall, C@MSN-P-A8 represses osteoclast differentiation and function by suppressing the expression of osteoclast-specific genes and interfering with NF-κB and MAPK signaling cascades in vitro.
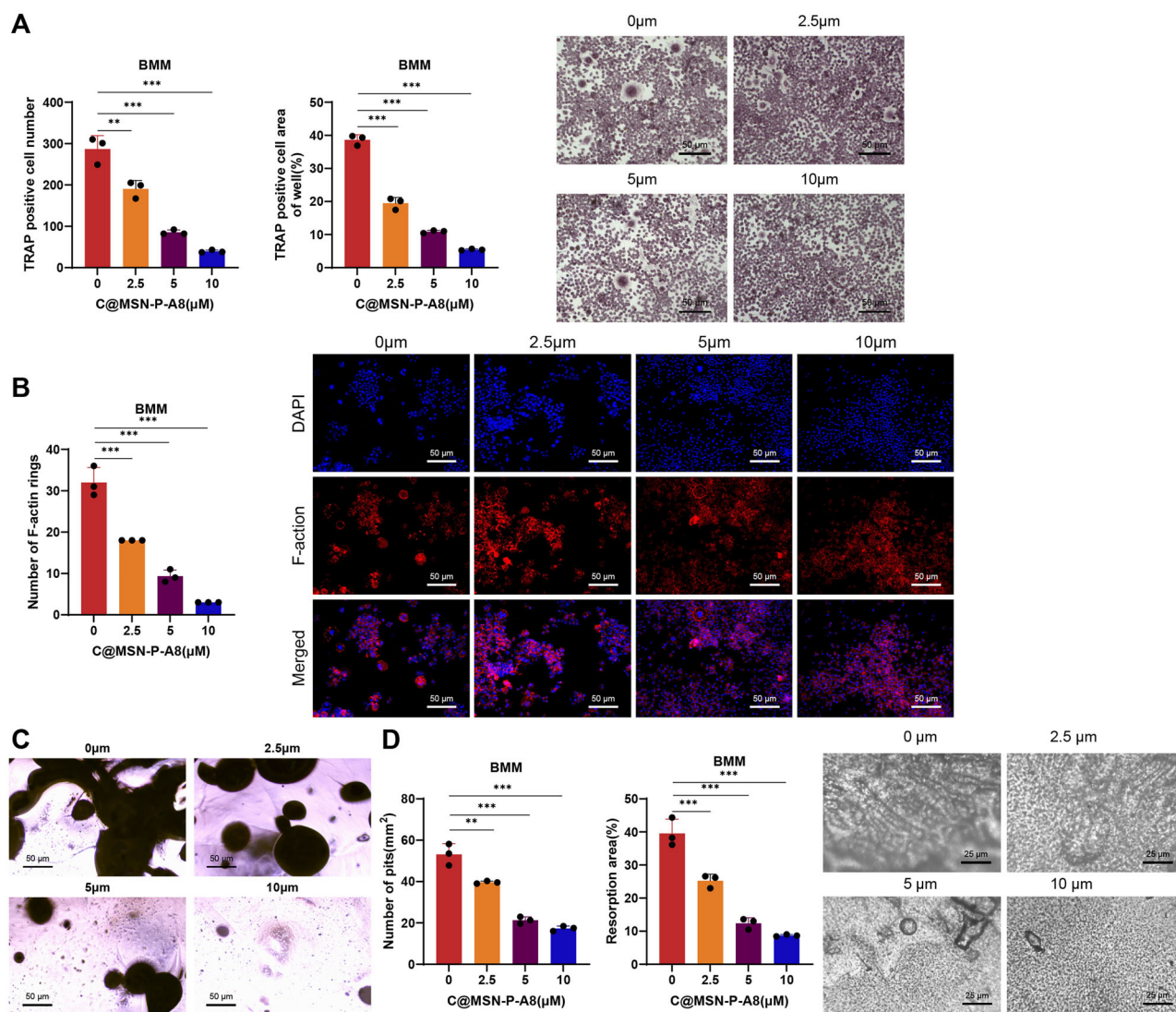
Fig. 3 | Impact of C@MSN-P-A8 on BMMs osteoclast formation and bone resorption. A TRAP staining to assess the effect of C@MSN-P-A8 on BMMs osteoclast formation (Scale bar = 50 μm). **B** Immunofluorescence analysis to investigate the influence of C@MSN-P-A8 on F-actin rings in BMMs (Scale bar = 50 μm). **C** Representative images stained using toluidine blue (Scale bar = 50 μm). **D** Bone resorption pit assay to determine the effect of C@MSN-P-A8 on BMMs osteoclast bone resorption function (Scale bar = 25 μm). * indicates comparison between two groups, **$P < 0.01$, ***$P < 0.001$, each cell experiment was performed in triplicate.

C@MSN-P-A8 alleviates ovariectomy-induced OP in rats in vivo

The ovariectomy-induced OP rat model is widely recognized for mimicking postmenopausal OP in humans. To evaluate the therapeutic efficacy of C@MSN-P-A8, we employed this model and conducted a series of in vivo assessments.

Micro-CT analysis of femoral bone demonstrated that rats in the OP group exhibited notable bone loss relative to the Sham group. This was evidenced by decreased BMD, BV/TV, Tb.N, and Tb.Th, alongside an increase in Tb.Sp. While the MSN-P-A8 group showed no notable improvement, both the Celastrol and C@MSN-P-A8 treatment groups demonstrated enhanced bone microarchitecture. Notably, C@MSN-P-A8 treatment led to more pronounced improvements in all measured parameters (Fig. 6A).

H&E staining further supported these findings. The OP group exhibited sparse, thin trabeculae, disrupted trabecular organization, extensive bone loss pits, and reduced cortical bone thickness. The MSN-P-A8 group showed minimal restoration of structure. In contrast, treatment with either Celastrol or C@MSN-P-A8 significantly improved trabecular morphology. Femoral trabeculae became more continuous and organized, with reduced

bone loss regions, and the therapeutic effect of C@MSN-P-A8 was more evident than that of free Celastrol (Fig. 6B).

Furthermore, TRAP staining revealed a substantial increase in multinucleated osteoclasts in the OP group, consistent with enhanced bone resorption. No significant reduction was observed in the MSN-P-A8 group. However, both Celastrol and C@MSN-P-A8 treatments led to a marked decrease in TRAP-positive osteoclasts, with C@MSN-P-A8 demonstrating a more robust anti-osteoclastic effect (Fig. 6C). Additionally, histological examination of major organs demonstrated no pathological alterations in any treatment group, including those receiving C@MSN-P-A8. All tissues maintained normal architecture, suggesting excellent systemic biocompatibility of the nanoplatform (Supplementary Fig. 2).

In conclusion, these results suggest that C@MSN-P-A8 suppresses ovariectomy-induced OP in rats.

Discussion

This study delves into the mechanisms concerning the therapeutic significance of C@MSN-P-A8, focusing on its modulation of the NF-κB
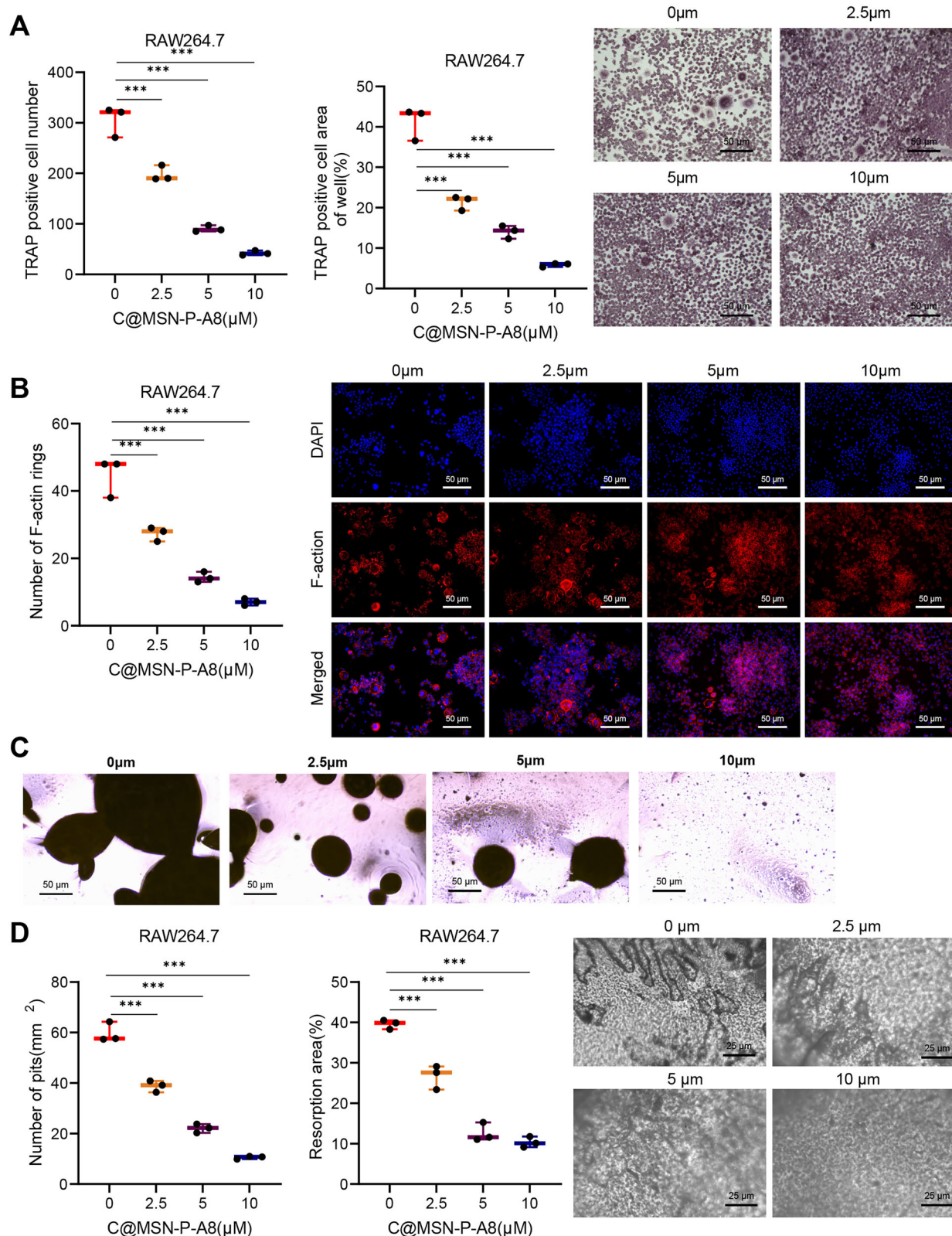
Fig. 4 | Impact of C@MSN-P-A8 on RAW264.7 osteoclast formation and bone resorption. A TRAP staining to assess the effect of C@MSN-P-A8 on RAW264.7 osteoclast formation (Scale bar = 50 μm). **B** Immunofluorescence analysis of the influence of C@MSN-P-A8 on the F-actin ring in RAW264.7 cells (Scale bar = 50 μm); **C** Representative images stained using toluidine blue (Scale bar = 50 μm); (**D**) Bone resorption pit assay evaluating the effect of C@MSN-P-A8 on osteoclast bone resorption function (Scale bar = 25 μm). * indicates comparison between the two groups, ***$P < 0.001$. The cell experiments were performed in triplicate.
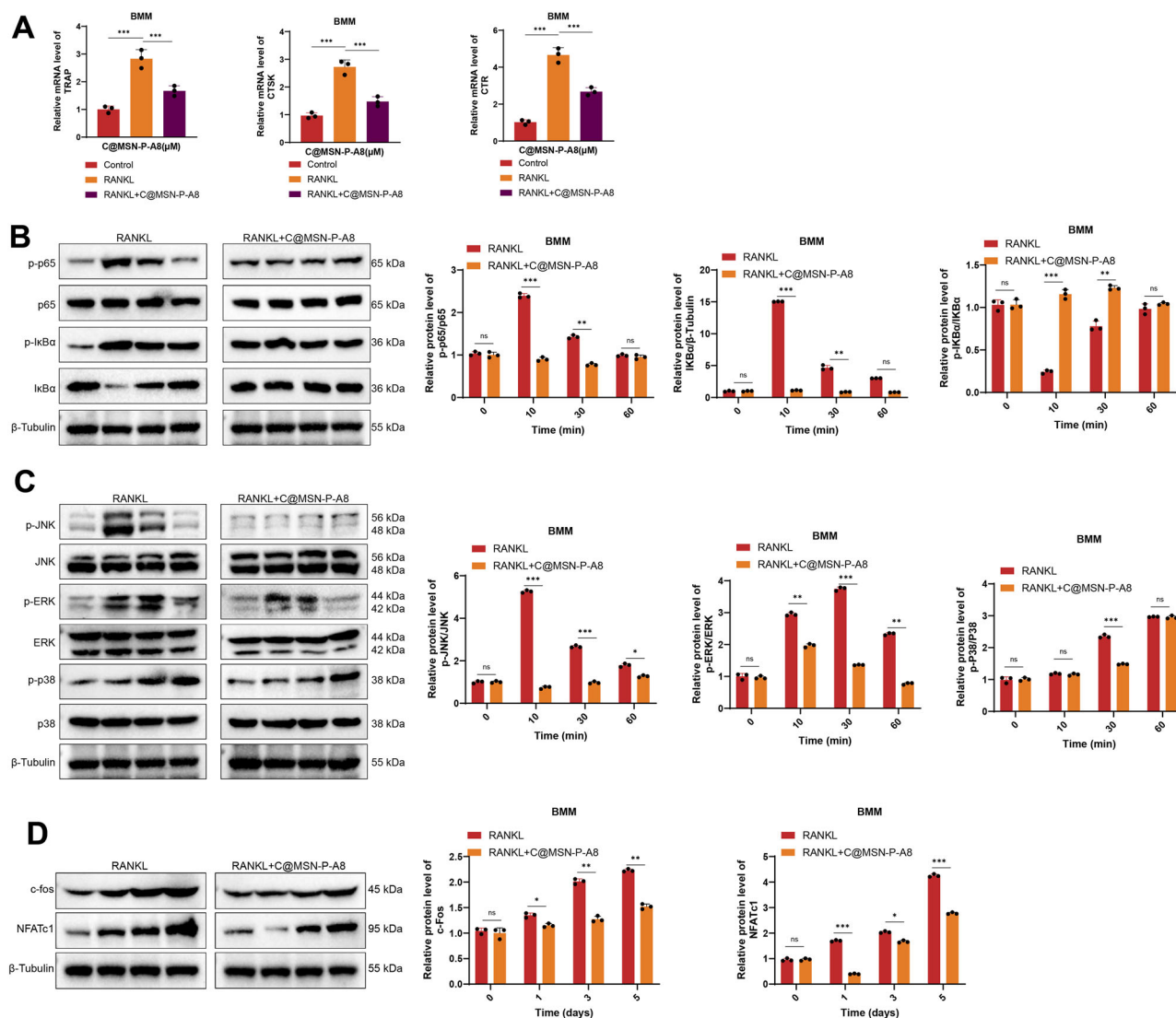
Fig. 5 | Impact of C@MSN-P-A8 on BMM osteoclast-specific gene expression and the NF-κB and MAPK signaling pathways. A RT-qPCR analysis of osteoclast-specific gene expression levels of CTSK, TRAP, and CTR mRNA in each group. **B** Western blot assessment of the expression levels of p-IκBα and p-p65 proteins in the NF-κB pathway in each group of cells. **C** Western blot analysis of the expression levels of p-JNK, p-ERK, and p-p38 proteins in the MAPK pathway in each group of cells. **D** Western blot analysis of the protein expression levels of c-fos and NFATc1 in each group of cells. 'ns' indicates no significant difference between the two groups, * represents comparison between the two groups, *$P < 0.05$, **$P < 0.01$, ***$P < 0.001$. The cell experiments were conducted in triplicate.

and MAPK pathways in managing OP. Compared to previous work, our study provides a more comprehensive analysis of the signaling-level interactions through which C@MSN-P-A8 inhibits osteoclast differentiation and bone resorption, offering deeper mechanistic insights into its potential as an anti-osteoporotic agent. In vitro experiments confirmed that C@MSN-P-A8 effectively suppresses osteoclast formation and bone resorption, findings that are consistent with prior studies on Celastrol and related nanomaterials[37–39]. However, unlike earlier work, our research delves further into the specific roles of the NF-κB and MAPK pathways, which are central to osteoclastogenesis. Our results report additional evidence for the regulatory effects of C@MSN-P-A8 on these signaling pathways and offer mechanistic insights into its role in suppressing osteoclast differentiation[40–42], and further validate C@MSN-P-A8 as a refined and more effective delivery platform[43,44].

In the in vivo OVX rat model, C@MSN-P-A8 treatment significantly improved bone microarchitecture, as shown by micro-CT and histological assessments. These results align well with previous research on Celastrol-based therapies[23–26], but our study further demonstrates that the PEG-Asp8-

modified MSNs substantially enhance bone-targeting specificity and sustained drug release compared to Celastrol alone. This highlights the value of smart nanocarrier systems in improving pharmacodynamics and site-specific therapeutic effects.

Based on these findings and existing literature, we propose that C@MSN-P-A8 alleviates postmenopausal OP primarily through suppression of the NF-κB and MAPK signaling axes, positioning it as a promising candidate for future OP therapies. This approach may offer a safer and more effective alternative to conventional treatments and lays the groundwork for novel clinical strategies in managing postmenopausal bone loss. Nonetheless, several limitations of this study should be reported. The current research is based on animal models and short-term observation periods, and lacks data from long-term evaluations or clinical trials. Furthermore, while our study focuses on key nodes within the NF-κB and MAPK pathways, it does not comprehensively explore upstream components such as IKK kinases, whose roles in response to C@MSN-P-A8 treatment remain to be clarified.

In summary, this study provides new mechanistic evidence that C@MSN-P-A8 effectively represses osteoclastogenesis and bone resorption
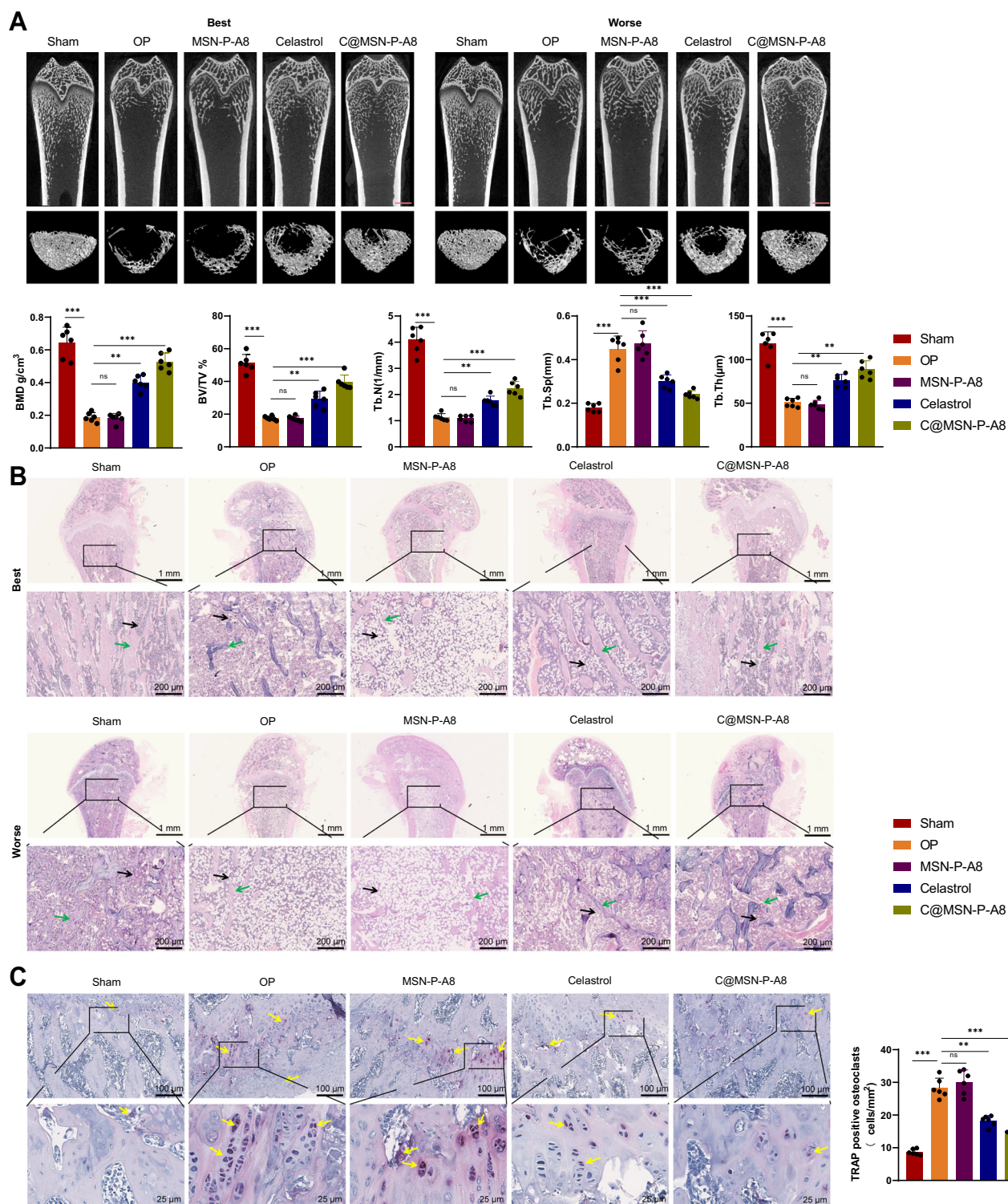
Fig. 6 | Impact of C@MSN-P-A8 on bone loss in osteoporotic rats. A Micro-CT image and statistical analysis of three-dimensional reconstruction for bone parameters, including BMD, BV/TV, Tb. Th, Tb. Sp, and Tb. N in each group of rats. The left image represents the best-case sample, and the right image represents the worst-case sample within each group, along with statistical analysis of bone parameters (Scale bar = 1 mm). **B** Representative H&E-stained images of rat femurs with green arrows indicating trabeculae and black arrows indicating bone marrow cavities (Scale bar=1 mm/200 μm). The left image represents the best-case sample, and the right image represents the worst-case sample within each group, along with statistical analysis of bone parameters. **C** Representative TRAP-stained images of rat femurs and quantitative analysis of osteoclast numbers on each bone surface (Scale bar = 100/25 μm). Yellow arrows represent osteoclasts. 'ns' indicates no significant difference between the two groups, * represents comparison between the two groups, **$P < 0.01$, ***$P < 0.001$. Each group consisted of six mice.

by targeting the NF-κB and MAPK axes. These findings not only support the continued development of bone-targeted Celastrol nanotherapies but also contribute valuable knowledge toward the molecular regulation of OP. Future research shoul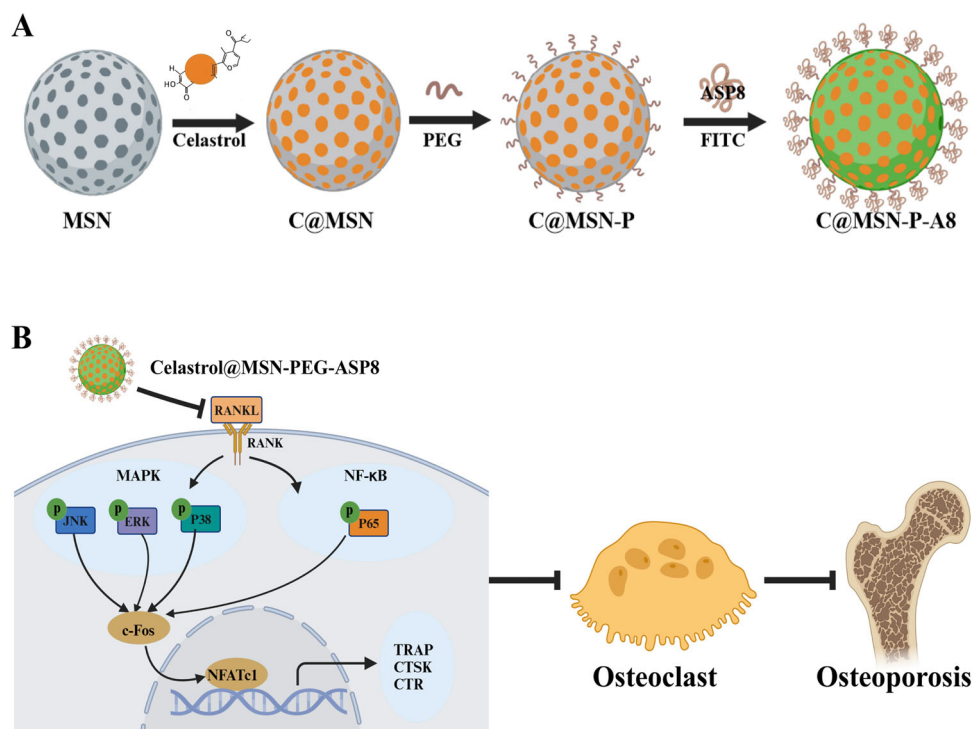d expand on these findings through long-term, multi-model, and potentially clinical investigations, aiming to optimize treatment efficacy and safety.

In summary, this study demonstrates that the bone-targeted nano sustained-release system C@MSN-P-A8 effectively alleviates OP in

Fig. 7 | Synthesis of C@MSN-P-A8 and its molecular mechanism in osteoporosis treatment.
A Synthesis process of Bone-Targeted Nano Sustained Release Materials C@MSN-P-A8.
B Molecular mechanism schematic of C@MSN-P-A8 for preventing and treating postmenopausal osteoporosis by inhibiting osteoclast formation and bone resorption through the suppression of the NF-κB and MAPK signaling pathways.

ovariectomized rats by inhibiting osteoclast formation and bone-resorptive function (Fig. 7). Through a series of cellular and animal experimentations, we systematically revealed the therapeutic potential and underlying mechanisms of C@MSN-P-A8 in OP treatment. In vitro, C@MSN-P-A8 significantly suppressed RANKL-induced osteoclast differentiation, which was mechanistically linked to the blockage of the NF-κB and MAPK pathways. Specifically, C@MSN-P-A8 reduced the degradation of IκBα and decreased the phosphorylation levels of JNK, ERK, and p38, indicating its regulatory role in blocking osteoclastogenic signaling cascades. In vivo, administration of C@MSN-P-A8 in an OVX rat model significantly improved bone mass and microarchitecture. Compared to the untreated OP group, treated animals exhibited higher bone density and reduced osteoclast activity, highlighting the material's osteoprotective efficacy. These findings suggest that C@MSN-P-A8 not only inhibits osteoclast function but also exemplifies the potential of nanotechnology-enabled targeted drug delivery systems for sustained and precise therapeutic intervention in bone disorders.

Despite these promising results, the study contains several limitations. The long-term biocompatibility and systemic stability of C@MSN-P-A8 remain to be fully evaluated in diverse biological contexts. Furthermore, the absence of direct comparisons with established antiresorptive agents, such as RANKL inhibitors, limits the assessment of its relative therapeutic potency. The impact of C@MSN-P-A8 on hormone levels, which are crucial in postmenopausal OP, was also not addressed. Future studies should aim to validate the long-term efficacy and safety of C@MSN-P-A8 in extended preclinical models, directly compare its performance with clinically approved treatments, investigate hormonal regulation and systemic metabolic effects, and optimize nanocarrier design and drug loading strategies to enhance therapeutic index while minimizing off-target toxicity.

Methods
Preparation of bone-targeted nano sustained-release materials C@MSN-P-A8
The synthesis of MSNs was performed following established protocols[45]. Briefly, 100 mg of cetyltrimethylammonium bromide (CTAB) was dissolved in 50 mL of deionized water, and 0.35 mL of 2 M NaOH solution was added under stirring. The mixture was heated to 70 °C, after which 0.5 mL of tetraethyl orthosilicate (TEOS; T110595-100ml, Aladdin, USA) was added dropwise. Subsequently, 0.5 mL of ethyl acetate was introduced, followed by stirring for 30 s and aging at 70 °C for 2 h. The resulting precipitate was harvested, washed with ethanol, and subjected to reflux in 10% (v/v) hydrochloric acid/ethanol solution at 78 °C for 6 h to remove CTAB, yielding purified MSNs[46].

To obtain amino-functionalized MSNs (MSN-NH₂), MSN (1 g) was redispersed in 100 mL of anhydrous ethanol. Then, 1 mL of APTMS was gradually added, and the suspension was stirred for 12 h. The functionalized nanoparticles were harvested by centrifugation at 5000 rpm for 25 min and repeatedly rinsed with deionized water to eliminate excess APTMS. The resulting MSN-NH₂, bearing with amino groups on both internal and external surfaces, was dried under vacuum[47]. For drug loading, 50 mg of MSN-NH₂ was suspended in 10 mL of methanol containing 35 mg of Celastrol (HY-13067, MedChemExpress, China). The mixture was shaken at 25 °C for 4 h. The Celastrol-loaded nanoparticles (C@MSN) were then isolated via centrifugation at 10,000 rpm, and any loosely bound surface drug was removed by washing with distilled water[48].

To functionalize the particles with polyethylene glycol (PEG), C@MSN was dispersed in 10 mL of water containing 28 mg of silane-PEG-COOH (S164249-100mg, Aladdin, USA), followed by addition of 0.2 mL of ammonia solution. The suspension was stirred for 4 h and centrifuged at 10,000 rpm, followed by trice washes to obtain PEGylated particles (C@MSN-P). Subsequently, 30 mg of C@MSN-P was suspended in 5 mL of MES buffer. To activate carboxyl groups, 5 mg of EDC (22980, ThermoFisher, USA) and 3.8 mg of NHS (24500, ThermoFisher, USA) were reacted for 30 min. Subsequently, 5 mg of Asp8 peptide (Shanghai Top-peptide Biotechnology Co., Ltd., China) was introduced, and the mixture was stirred for 2 h. The final bone-targeted nanoparticles (C@MSN-P-A8) were harvested by centrifugation at 10,000 rpm and washed thoroughly with deionized water.

For fluorescence tracking, the particles were labeled with fluorescent dye fluorescein isothiocyanate (FITC, HY-66019, MedChemExpress, China). FITC was dissolved in methanol (1 mg/mL), and 500 μL of this solution was supplemented to the methanol suspension of nanoparticles, which was stirred overnight at ambient temperature. Unbound FITC was

eliminated by centrifugation at 7000 rpm, followed by repeated washing with ultrapure water. The FITC-labeled nanoparticles were stored at 4 °C[49].

Characterization of bone-targeted nano-sustained-release materials C@MSN-P-A8

The morphology and ultrastructure of MSN, C@MSN, and C@MSN-P-A8 were examined using transmission electron microscopy (TEM; JEM2010, JEOL, Tokyo, Japan). To evaluate surface area and pore characteristics, nitrogen adsorption-desorption isotherms were gained utilizing a Micromeritics porosity analyzer (Norcross, USA). The Brunauer-Emmett-Teller (BET) method was employed to calculate specific surface area, while pore size distribution and volume were assessed using the Barrett-Joyner-Halenda (BJH) model. Particle size distribution and hydrodynamic diameter of the samples were determined via dynamic light scattering (DLS) at 298 K with the help of a Zetasizer Nano instrument (Malvern Instruments, UK). The sample's thermal decomposition profile and compositional features were examined using thermogravimetric analysis (TGA 209F1, Netzsch, Germany). The analysis was carried out under an inert nitrogen atmosphere with temperature ramping at 10 °C per minute (Netzsch, Germany)[45,48].

Drug release assessment

To evaluate the release kinetics of Celastrol, 5 mL of either C@MSN or C@MSN-P-A8 dispersion was enclosed in a dialysis membrane (MWCO: 3000 Da) and incubated in phosphate-buffered saline (PBS, pH 7.4). The setup was maintained at 37 °C with gentle agitation at 100 rpm using a thermostatic shaker. At designated time points, 1 mL of the external medium was collected and immediately replenished with an equal volume of fresh PBS to preserve sink conditions. The amount of Celastrol released was determined via inductively coupled plasma atomic emission spectroscopy (ICP-AES)[45,50].

In vivo bone-targeting characteristics of C@MSN-P-A8

Three-month-old female Sprague-Dawley (SD) rats, weighing 220–260 g, were obtained from Vital River Laboratory Animal Technology Co., Ltd. (Beijing, China) and housed under SPF conditions with controlled temperature (22–25 °C), humidity (45–60%), and a 12-h light/dark cycle. Chow and water were supplied freely for the duration of the experiment. After a week of acclimatization, they were monitored for health status. All procedures were granted by the Animal Ethics Committee of the First Affiliated Hospital of Nanchang University, in compliance with institutional and national guidelines for the care and use of laboratory animals.

Twenty-four rats were randomized into MSN, C@MSN, C@MSN-P, and C@MSN-P-A8 groups (n = 6 per group). Each group received a single tail vein injection of the corresponding nanoparticle formulation at a dose of 50 mg/kg. At 4 and 72 h post-injection, animals were anesthetized with 3% isoflurane for induction and maintained at 1.5–2.5% isoflurane via inhalation, with anesthetic depth continuously assessed based on respiratory patterns and absence of reflexes. To ensure unconsciousness during euthanasia, an overdose of isoflurane (≥ 5% in oxygen) was administered until complete cessation of cardiac and respiratory activity. Humane endpoints were defined as >20% body weight loss, persistent inability to access food or water, or signs of severe distress such as labored breathing or lethargy. Animals were monitored daily for general health, with monitoring increased to twice daily if any signs of severe illness were observed. After euthanasia, major organs—including the heart, liver, spleen, lungs, kidneys, and femurs—were harvested. Fluorescence distribution in each organ was visualized using a fluorescence imaging system to assess the biodistribution and bone-targeting efficacy of the formulations[36,45].

CCK-8

BMMs (1×10^4/well) were plated in 96-well plates and pre-cultured for 24 h in α-MEM enriched with 15% FBS, 1% penicillin-streptomycin, and 30 ng/mL macrophage colony-stimulating factor (M-CSF). After attachment, cells were exposed to C@MSN-P-A8 at varying concentrations (0, 1.25, 2.5, 5, 10, 20, 40, and 80 μM) for another 24 h. Cell viability was tested utilizing CCK-8 assay (Solarbio, CA1210).

Similarly, RAW264.7 cells were seeded at 3×10^3 cells per well in 96-well plates and cultured in DMEM containing 15% FBS and 1% penicillin-streptomycin. Following 24 h of incubation, the cells were exposed to the same gradient of C@MSN-P-A8 concentrations for 24 h.

Following treatment, 10 μL of CCK-8 reagent was supplemented for 2-h of incubation at 37 °C in a 5% CO_2 incubator. The absorbance at 450 nm was examined utilizing a microplate reader to determine cell viability[51].

Immunofluorescence detection of F-actin ring

To visualize osteoclast cytoskeletons, RAW264.7 or BMMs were seeded onto sterile glass coverslips in 24-well plates. Once fused, cells were treated with 50 ng/mL receptor activator of nuclear factor κB ligand (RANKL) and C@MSN-P-A8 at 0, 2.5, 5, or 10 μM until mature osteoclasts appeared in control wells. Fixation was performed using 4% paraformaldehyde (20 min, RT), followed by 0.1% Triton X-100 permeabilization (5 min) and PBS washes. F-actin was labeled with TRITC-phalloidin (40734ES75, Yeasen), and nuclei were counterstained with DAPI. Coverslips were mounted using ProLong™ Diamond (Invitrogen) and imaged by confocal microscopy (LSM5, Zeiss). F-actin ring structures were quantified utilizing ZEN software to assess osteoclast formation and cytoskeletal organization[36,52].

Bone resorption pit assay

Bovine bone slices were placed into 96-well plates, and osteoclast precursors (2.5×10^5 cells/well) were seeded and cultured in appropriate media at 37 °C for at least 14 days to allow formation of mature osteoclasts. Following incubation, cells were removed by sonicating the wells in 250 μL of 70% isopropanol for at least 15 min. The bone slices were then stained with 1% toluidine blue (100 μL per slice) for 2 min at ambient temperature. Residual dye was removed by rinsing the slices five times with 250 μL of Milli-Q water. Resorption pits, which appeared as dark blue regions, were visualized and quantified under a light microscope or using bone morphometric analysis software[53].

In our experiments, RAW264.7 or BMM cells were seeded onto bovine bone slices in 96-well plates and cultured in complete DMEM containing 50 ng/mL RANKL to induce osteoclast differentiation. Cells were subjected to C@MSN-P-A8 treatment (0, 2.5, 5, and 10 μM) and maintained for 5 days. Following treatment, cells were mechanically eliminated from the bone surfaces, and the slices were analyzed utilizing scanning electron microscopy (SEM; FEI Quanta 250), followed by quantification utilizing ImageJ software (NIH, Bethesda, MD)[23,54].

Quantification of target gene expression by RT-qPCR

RAW264.7 and BMMs were cultured in 6-well plates with 50 ng/mL RANKL and treated with 10 μM C@MSN-P-A8 for 5 days. Total RNA was extracted employing TRIzol (ThermoFisher, 15596026), and quality was assessed via NanoDrop LITE (260/280 nm). cDNA was synthesized with PrimeScript RT (TaKaRa, RR047Q). qPCR was run on a 7500 Fast system (ThermoFisher, 4351106) using TaKaRa-supplied primers (sequences listed in Supplementary table 1). GAPDH served as the normalizer. Transcript levels were normalized using the $2^{-\Delta\Delta Ct}$ method[55–57].

Rat OP model and experimental procedures

After a week of acclimatization, all rats were anesthetized via intraperitoneal injection of 3% pentobarbital sodium (30–40 mg/kg). Under deep anesthesia, animals were positioned on a sterile surgical platform, and dorsal abdominal hair was shaved. A longitudinal incision (~ 1 cm) was prepared approximately 0.5 cm below the rib arch on the dorsal side. Skin and muscle were dissected to expose the ovaries, which were excised bilaterally after ligating the fallopian tubes. Wounds were closed in layers with sutures. Sham-operated rats underwent fat pad removal near the ovaries without ovary excision. Postoperative care included topical application of erythromycin ointment at the incision site to prevent infection. Beginning on

the second postoperative day, daily vaginal smears were collected for one week to confirm successful ovariectomy.

Rats were randomized into Sham group, OP group, Celastrol group, MSN-PEG-ASP8 (MSN-P-A8) group, and C@MSN-P-A8 group (n = 6 per group). From the ninth postoperative week, each group received daily treatments via intraperitoneal injection for four consecutive weeks based on body weight. Specifically, the Sham and OP groups received intraperitoneal injections of saline, the Celastrol group received Celastrol (20 mg/kg/dose) intraperitoneally daily, the MSN-P-A8 group received (50 mg/kg/dose) intraperitoneally daily, and the C@MSN-P-A8 group received (50 mg/kg/dose) intraperitoneally daily. At the end of the study, rats were re-anesthetized and euthanized via inhalation of an overdose of isoflurane ($\geq 5\%$ in oxygen) until cessation of cardiac and respiratory activity, ensuring unconsciousness at the time of euthanasia. Humane endpoints included >20% body weight loss, persistent inability to eat or drink, or signs of severe distress such as labored breathing or lethargy. Animals were monitored daily, with twice-daily monitoring if signs of severe illness were observed. Subsequently, bilateral femurs, tibias, lumbar vertebrae, and major organs (heart, liver, spleen, lungs, kidneys, and brain) were harvested. For histological and micro-computed tomography (micro-CT) analysis, the right femur was selected to ensure consistency and reduce inter-sample variability. Samples were fixed in 4% paraformaldehyde for subsequent imaging and histopathological evaluation[58–60]. For in vivo fluorescence biodistribution studies, nanoparticles were labeled with fluorescein isothiocyanate (FITC; HY-66019, MedChemExpress, China). Imaging was implemented utilizing the Kodak F PRO fluorescence imaging system (Kodak, USA) with excitation/emission wavelengths of 495/519 nm. The fluorescence distribution of FITC-labeled MSN, C@MSN, C@MSN-PEG, and C@MSN-P-A8 in harvested organs was analyzed. Quantitative fluorescence intensity was measured using Kodak Molecular Imaging Software version 5.X[47].

Micro-CT scanning and bone histomorphometric analysis

Following euthanasia, femurs from each experimental group were aseptically harvested and fixed in 4% paraformaldehyde for 48 h. The samples were then rinsed with running tap water for 24 h prior to imaging. High-resolution micro-CT was performed using the mCT80 scanner (Scanco Medical, Switzerland). Scanning parameters were set as follows: 1 mm aluminum filter, 55 kV voltage, 100 µA current, 14-min scanning time, 180° rotation, frame averaging of 1–2, and an image resolution of 6–8 µm. Three-dimensional reconstructions were generated using NRecon software (Micro Photonics, USA). Quantitative static histomorphometric analyses were conducted to evaluate bone microarchitecture. The following parameters were measured: bone mineral density (BMD), bone volume fraction (bone volume/tissue volume, BV/TV), trabecular thickness (Tb.Th), trabecular separation (Tb.Sp), and trabecular number (Tb.N)[58,59].

Histological analysis

For histological evaluation, femurs were fixed in 4% paraformaldehyde for 24 h and subsequently decalcified in 10% ethylenediaminetetraacetic acid (EDTA) for 4 weeks at ambient temperature. After decalcification, tissues were dehydrated, embedded in paraffin, and sectioned into 5 µm-thick slices using a microtome.

Hematoxylin and eosin (H&E) staining (PT001, Bogu Bio) was applied to bone samples to reveal structural and cytological features.

Tartrate-resistant acid phosphatase (TRAP) staining was utilized to evaluate osteoclast formation. Sections were stained using a commercial TRAP staining kit (G1492, Solarbio, China),. and nuclei were counter-stained with hematoxylin. TRAP-positive multinucleated osteoclasts were identified and quantified under light microscopy[58,59].

Western blot analysis

Proteins were isolated in RIPA buffer with PMSF (Beyotime, P0013C), quantified via BCA assay (ThermoFisher, 23227), and 50 µg per sample was heat-denatured and resolved by SDS-PAGE. Gels were transferred onto polyvinylidene difluoride membranes (ThermoFisher, 88518), blocked with 5% BSA (Sigma) for 1 h, and incubated overnight at 4 °C with primary antibodies (dilution 1:1000 unless otherwise stated): rabbit anti-p65 (phospho S536) (ab76302, Abcam, UK), rabbit anti-p65 (PA5-16545, ThermoFisher, USA), rabbit anti-IKBα (ab32518, Abcam, UK), rabbit anti-IKBα (phospho S36) (ab133462, Abcam, UK), rabbit anti-JNK (phospho T183 + Y185) (ab307802, Abcam, UK), rabbit anti-JNK (ab199380, Abcam, UK), rabbit anti-ERK (ab109282, Abcam, UK), rabbit anti-p-ERK (Thr202, Tyr204) (MA5-47641, ThermoFisher, USA), mouse anti-p38 (33-1300, ThermoFisher, USA), mouse anti-p-p38 (Thr180, Tyr182) (1:2000, MA5-15218, ThermoFisher, USA), mouse anti-c-Fos (ab208942, Abcam, UK), rabbit anti-NFATc1 (PA5-79730, ThermoFisher, USA), and mouse anti-β-Tubulin (ab6046, Abcam, UK). Following three TBST washes (10 min each), the membrane was incubated for 1 h at ambient temperature with HRP-conjugated secondary antibodies: goat anti-rabbit IgG H&L (ab97051) and goat anti-mouse IgG (ab6789), both at 1:2000 dilution (Abcam, UK). Signal detection was carried out using an ECL chemiluminescent kit (abs920, Aibosi, Shanghai, China). Band intensities were normalized to β-Tubulin and quantified using Quantity One (v4.6.2). All experiments were repeated in triplicate, and mean values were used for statistical comparison[61].

Statistical analysis

All statistical analyses were implemented utilizing SPSS 22.0 (SPSS Inc., Chicago, USA) and GraphPad Prism 9.5 (GraphPad Software, USA). Data are detailed as mean ± standard deviation (SD). For comparisons between two groups, unpaired Student's t tests were used. One-way analysis of variance was applied for comparisons among multiple groups. Prior to hypothesis testing, data normality was assessed utilizing the Shapiro-Wilk test, and variance homogeneity was checked via the Levene test. For data with equal variances, Dunnett's t test or LSD t test was selected for pairwise comparisons. When variance homogeneity was not satisfied, Dunnett's T3 test was employed. A p value < 0.05 was deemed statistically significant.

Data availability

The datasets used or analyzed during the current study are available from the corresponding author on reasonable request.

References

1. LeBoff, M. S. et al. The clinician's guide to prevention and treatment of osteoporosis. *Osteoporos. Int* **33**, 2049–2102 (2022).
2. Yong, E. & Logan, S. Menopausal osteoporosis: screening, prevention and treatment. *Singapore Med. J.* **62**, 159–166 (2021).
3. Ayers, C. et al. Effectiveness and safety of treatments to prevent fractures in people with low bone mass or primary osteoporosis: a living systematic review and network meta-analysis for the American College of Physicians. *Ann. Intern. Med.* **176**, 182–195 (2023).
4. ACOG Committee on Clinical Practice Guidelines–Gynecology Management of postmenopausal osteoporosis. *Obstet. Gynecol.* **139**, 698–717 (2022).
5. Gosset, A., Pouillès, J. M. & Trémollieres, F. Menopausal hormone therapy for the management of osteoporosis. *Best. Pract. Res. Clin. Endocrinol. Metab.* **35**, 101551 (2021).
6. Noirrit-Esclassan, E. et al. Critical role of estrogens on bone homeostasis in both male and female: from physiology to medical implications. *IJMS* **22**, 1568 (2021).
7. Ma, B. et al. Causal associations of anthropometric measurements with fracture risk and bone mineral density: a mendelian randomization study. *J. Bone Miner. Res.* **36**, 1281–1287 (2020).
8. Li, H. L. et al. Relationship between bone mineral density and fragility fracture risk: a case-control study in Changsha, China. *BMC Musculoskelet. Disord.* **22**, 728 (2021).

9. Fatima, K. et al. Relationship between renal function and bone mineral density in postmenopausal women. *Mymensingh Med. J.* **32**, 144–152 (2023).

10. Gopaul, A. et al. Denosumab in chronic kidney disease: a narrative review of treatment efficacy and safety. *Arch. Osteoporos.* **16**, 116 (2021).

11. Méndez-Sánchez, L. et al. Calcium and vitamin D for increasing bone mineral density in premenopausal women. *Cochrane Database Syst. Rev.* **1**, CD012664 (2023).

12. Reid, I. R. Extensive expertise in endocrinology: osteoporosis management. *Eur. J. Endocrinol.* **187**, R65–R80 (2022).

13. Feng, F. et al. Comprehensive interventions including vitamin D effectively reduce the risk of falls in elderly osteoporotic patients. *Orthop. Surg.* **13**, 1262–1268 (2021).

14. Tanakol, R., Gül, N., Üzüm, A. K. & Aral, F. Calcitriol treatment in patients with low vitamin D levels. *Arch. Osteoporos.* **13**, 114 (2018).

15. Rahme, M. et al. Impact of calcium and two doses of vitamin d on bone metabolism in the elderly: a randomized controlled trial. *J. Bone Miner. Res.* **32**, 1486–1495 (2017).

16. Mesinovic, J. et al. Effect of 16-weeks vitamin D replacement on calcium-phosphate homeostasis in overweight and obese adults. *J. Steroid Biochem. Mol. Biol.* **186**, 169–175 (2019).

17. Munshi, R. P., Kumbhar, D. A., Panchal, F. H. & Varthakavi, P. Assessing the effectiveness ofpanchatikta ghrita, a classical ayurvedic formulation as add-on therapy to vitamin d3and calcium supplements in patients with osteopenia: a randomized, open-labeled, comparative, controlled clinical study. *J. Altern. Complement. Med.* **25**, 1044–1053 (2019).

18. Ilich, J. Z. et al. Role of calcium and low-fat dairy foods in weight-loss outcomes revisited: results from the randomized trial of effects on bone and body composition in overweight/obese postmenopausal women. *Nutrients* **11**, 1157 (2019).

19. Smith, L. M., Gallagher, J. C., Kaufmann, M. & Jones, G. Effect of increasing doses of vitamin D on bone mineral density and serum N-terminal telopeptide in elderly women: a randomized controlled trial. *J. Intern. Med.* **284**, 685–693 (2018).

20. Chiodini, I. & Bolland, M. J. Calcium supplementation in osteoporosis: useful or harmful?. *Eur. J. Endocrinol.* **178**, D13–D25 (2018).

21. Thiel, Y. et al. Antimicrobial peptide gene expression in medication-related osteonecrosis of the jaw. *Pathol. Res. Pract.* **216**, 153245 (2020).

22. ZAMAI, R. S. et al. Does resveratrol favor peri-implant bone repair in rats with ovariectomy-induced osteoporosis? Gene expression, counter-torque and micro-CT analysis. *Braz. oral. res* **37**, e003 (2023).

23. Xu, Q. et al. Celastrol attenuates RANKL-induced osteoclastogenesis in vitro and reduces titanium particle-induced osteolysis and ovariectomy-induced bone loss in vivo. *Front Pharm.* **12**, 682541 (2021).

24. Xi, J. et al. Celastrol inhibits glucocorticoid-induced osteoporosis in rat via the PI3K/AKT and Wnt signaling pathways. *Mol. Med. Rep.* https://doi.org/10.3892/mmr.2018.9436 (2018).

25. Li, L. et al. Celastrol regulates bone marrow mesenchymal stem cell fate and bone-fat balance in osteoporosis and skeletal aging by inducing PGC-1α signaling. *Aging* **12**, 16887–16898 (2020).

26. Yang, W. et al. Cryptotanshinone suppressed postmenopausal osteoporosis by preventing RANKL-mediated osteoclastogenesis against kidney injury. *Evid. Based Complement. Alternat. Med.* **2022**, 1–8 (2022).

27. Xu, W. et al. Sustained-release ketamine-loaded lipid-particulate system: in vivo assessment in mice. *Drug Deliv. Transl. Res* **12**, 2518–2526 (2021).

28. Andishmand, H. et al. Designing and fabrication of colloidal nano-phytosomes with gamma-oryzanol and phosphatidylcholine for encapsulation and delivery of polyphenol-rich extract from pomegranate peel. *Int. J. Biol. Macromol.* **256**, 128501 (2024).

29. Gong, S. et al. pH-responsive mesoporous silica nanoparticles loaded with naringin for targeted osteoclast inhibition and bone regeneration. *Int. J. Nanomed.* **19**, 6337–6358 (2024).

30. Arnst, J. et al. Bioactive silica nanoparticles target autophagy, NF-κB, and MAPK pathways to inhibit osteoclastogenesis. *Biomaterials* **301**, 122238 (2023).

31. Mora-Raimundo, P. et al. Osteoporosis remission and new bone formation with mesoporous silica nanoparticles. *Adv. Sci.* **8**, e2101107 (2021).

32. He, Y. et al. Preparation of targeted mitochondrion nanoscale-release peptides and their efficiency on eukaryotic cells. *J. Biomed. Nanotechnol.* **17**, 1679–1689 (2021).

33. Yu, F. et al. Studies of a novel bone-targeted nano drug delivery system with a HAP core-PSI coating structure for tanshinol injection. *J. Drug Target.* **31**, 762–775 (2023).

34. Shi, Y. et al. Morin attenuates osteoclast formation and function by suppressing the NF-κB, MAPK and calcium signalling pathways. *Phytother. Res.* **35**, 5694–5707 (2021).

35. Tao, H. et al. Urolithin A suppresses RANKL-induced osteoclastogenesis and postmenopausal osteoporosis by, suppresses inflammation and downstream NF-κB activated pyroptosis pathways. *Pharmacol. Res.* **174**, 105967 (2021).

36. Wang, J. et al. Neuregulin 1/ErbB4 signaling contributes to the anti-epileptic effects of the ketogenic diet. *Cell Biosci.* **11**, 29 (2021).

37. Yao, Z., Getting, S. J. & Locke, I. C. Regulation of TNF-induced osteoclast differentiation. *Cells* **11**, 132 (2021).

38. Yasuda, H. Discovery of the RANKL/RANK/OPG system. *J. Bone Min. Metab.* **39**, 2–11 (2021).

39. Veis, D. J. & O'Brien, C. A. Osteoclasts, master sculptors of bone. *Annu. Rev. Pathol. Mech. Dis.* **18**, 257–281 (2023).

40. Chen, Y. et al. Beneficial effects of natural flavonoids on neuroinflammation. *Front Immunol.* **13**, 1006434 (2022).

41. Li, N. et al. The anti-inflammatory actions and mechanisms of acupuncture from acupoint to target organs via neuro-immune regulation. *JIR* **14**, 7191–7224 (2021).

42. Li, X. H. et al. The signaling pathways and targets of natural compounds from traditional chinese medicine in treating ischemic stroke. *Molecules* **27**, 3099 (2022).

43. Zhou, Z. et al. Association between triglycerides and risk of dementia in community-dwelling older adults. *Neurology* **101**, e2288–e2299 (2023).

44. Luu, C. H., Nguyen, N. & Ta, H. T. Unravelling surface modification strategies for preventing medical device-induced thrombosis. *Adv. Healthc. Mater.* **13**, e2301039 (2023).

45. Yao, C. et al. A bone-targeting enoxacin delivery system to eradicate staphylococcus aureus-related implantation infections and bone loss. *Front. Bioeng. Biotechnol.* **9**, 749910 (2021).

46. Santhamoorthy, M. et al. Synthesis of functionalized mesoporous silica nanoparticles for colorimetric and fluorescence sensing of selective metal (Fe3+) ions in aqueous solution. *Methods* **223**, 26–34 (2024).

47. Khosraviyan, P. et al. Mesoporous silica nanoparticles functionalized with folic acid/methionine for active targeted delivery of docetaxel. *OTT* **9**, 7315–7330 (2016).

48. Jin, T. et al. Intra-articular delivery of celastrol by hollow mesoporous silica nanoparticles for pH-sensitive anti-inflammatory therapy against knee osteoarthritis. *J. Nanobiotechnol* **18**, 94 (2020).

49. Wang, J. et al. Mesoporous silica nanoparticles combined with MoS2 and FITC for fluorescence imaging and photothermal therapy of cancer cells. *J. Mater. Sci.* **55**, 15263–15274 (2020).

50. Choi, J. Y. et al. PEGylated polyaminoacid-capped mesoporous silica nanoparticles for mitochondria-targeted delivery of celastrol in solid tumors. *Colloids Surf. B: Biointerfaces* **165**, 56–66 (2018).

51. Huang, Y. F. et al. FIBP knockdown attenuates growth and enhances chemotherapy in colorectal cancer via regulating GSK3β-related pathways. *Oncogenesis* **7**, 77 (2018).
52. Zhang, Y. et al. ED-71 inhibited osteoclastogenesis by enhancing EphrinB2–EphB4 signaling between osteoclasts and osteoblasts in osteoporosis. *Cell. Signal.* **96**, 110376 (2022).
53. Vesprey, A. & Yang, W. Pit assay to measure the bone resorptive activity of bone marrow-derived osteoclasts. *Bio Protoc.* **6**, e1836 (2016).
54. Hu, L. et al. MiR-1224-5p modulates osteogenesis by coordinating osteoblast/osteoclast differentiation via the Rap1 signaling target ADCY2. *Exp. Mol. Med.* **54**, 961–972 (2022).
55. Ayuk, S. M., Abrahamse, H. & Houreld, N. N. The role of photobiomodulation on gene expression of cell adhesion molecules in diabetic wounded fibroblasts in vitro. *J. Photochem. Photobiol. B: Biol.* **161**, 368–374 (2016).
56. Wu, Q. & Yi, X. Down-regulation of long noncoding RNA MALAT1 protects hippocampal neurons against excessive autophagy and apoptosis via the PI3K/Akt signaling pathway in rats with epilepsy. *J. Mol. Neurosci.* **65**, 234–245 (2018).
57. Mao, Q., Liang, X. L., Zhang, C. L., Pang, Y. H. & Lu, Y. X. LncRNA KLF3-AS1 in human mesenchymal stem cell-derived exosomes ameliorates pyroptosis of cardiomyocytes and myocardial infarction through miR-138-5p/Sirt1 axis. *Stem Cell Res. Ther.* **10**, 393 (2019).
58. Chen, S. et al. Catalpol attenuates osteoporosis in ovariectomized rats through promoting osteoclast apoptosis via the Sirt6-ERα-FasL axis. *Phytomedicine* **123**, 155262 (2024).
59. Guo, M. et al. Lactobacillus rhamnosus GG ameliorates osteoporosis in ovariectomized rats by regulating the Th17/Treg balance and gut microbiota structure. *Gut Microbes* **15**, 2190304 (2023).
60. Liu, F. et al. Effect of Zuoguiwan on osteoporosis in ovariectomized rats through RANKL/OPG pathway mediated by β2AR. *Biomed. Pharmacother.* **103**, 1052–1060 (2018).
61. Jiang, M. et al. Regulation of PUMA-α by p53 in cisplatin-induced renal cell apoptosis. *Oncogene* **25**, 4056–4066 (2006).

Acknowledgements

Author contributions

Xiaolong Yu performed the majority of the experiments and data analysis and drafted the manuscript. Shengtao Zhang contributed to the nanoparticle synthesis and in vitro assays. Zhiqi Wei assisted with the in vivo experiments and histological analysis. Qiang Xu conceived and supervised the project, provided critical revisions to the manuscript, and secured funding. All authors reviewed and approved the final manuscript.

Competing interests

The authors declare no competing interests.

Additional information

Supplementary information The online version contains supplementary material available at https://doi.org/10.1038/s41538-025-00576-8.

Correspondence and requests for materials should be addressed to Qiang Xu.

Reprints and permissions information is available at http://www.nature.com/reprints

Publisher's note Springer Nature remains neutral with regard to jurisdictional claims in published maps and institutional affiliations.